Biosensors and Bioelectronics 296 (2026) 118324

Contents lists available at ScienceDirect

Biosensors and Bioelectronics

journal homepage: www.elsevier.com/locate/bios

Molecular tension tether based on electrochemiluminescence sensor for cellular mechanics measurement

Xiaofei Ma, Chen Zhao, Yongli Wu, Zhuoxin Ye, Pinyi Ma, Daqian Song, Ying Sun *

College of Chemistry, Jilin Province Research Center for Engineering and Technology of Spectral Analytical Instruments, Jilin University, Qianjin Street 2699, Changchun, 130012, PR China

ARTICLE INFO

Keywords:
Cellular mechanical forces
ECL sensor
Tension gauge tether (TGT)
Fibroblast

ABSTRACT

Cellular mechanical force, produced by actomyosin contractility and actin polymerization, are transmitted to extracellular matrix ligands and neighboring cells. It is essential for processes such as cell adhesion, migration, morphogenesis and differentiation. Here, we developed a molecular tension gauge tether (TGT) platform for measuring cellular mechanical force based on ultrasensitive electrochemical luminescence (ECL) sensor. It engaged TGT with cellular mechanical force-driven toehold-mediated strand displacement (F-TSDR) and catalytic hairpin assembly (CHA) amplification. When the integrin of the fibroblast membrane is successfully recognized by the integrin ligand (cRGDfk) in TGT, the duplex split irreversibly by cellular mechanical force. The F-TSDR and CHA amplification can be converted into ECL signals. Additionally, Pt@La-MOF with high ECL efficiency was used as the anode luminescent unit. During the F-TSDR process, if the cellular mechanical force exceeds the tension threshold (T_{tol}), the cell receptor effectively triggers mechanical denaturation of the S1-S2-RT1 probe (unzipping mode, T_{tol} ~12 pN) to release S2, the CHA cycle begins, leading to the quenching of the ECL signal from the luminescent unit ("on" to "off"). If the cellular mechanical force is below T_{tol} (shearing mode, T_{tol} ~56 pN). It does not trigger the structural denaturation of the S1-S2-RT2 probe to release S2, resulting in no ECL signal change. This work develops a model that converts cellular mechanical force into ECL signals, ranging from 12 to 56 pN. It provides a novel and highly sensitive ECL sensor for cellular mechanical force measurement on cellular metastasis research and anti-adhesion drug screening.

1. Introduction

Cellular mechanical forces (Huse, 2017), also called cellular adhesion forces (Yang et al., 2025), are the force that causes cells to bind to each other or to the extracellular matrix (ECM) through adhesion receptors such as integrins (Sun et al., 2019), selectins (Moog et al., 2016), immunoglobulin superfamily members (Jimbo et al., 2020), and cadherins (Medina et al., 2023). These mechanical force signals, measured in the pN range, pass through the cell membrane via transmembrane receptors (Hu et al., 2023). Their roles include mediating adhesion (Zhong et al., 2023), participating in signal transduction (Elosegui-Artola et al., 2016), inflammation, tumor metastasis, and immune recognition. Therefore, advancing technologies to measure mechanical forces applied to living cell membrane receptors is crucial for deciphering the molecular mechanisms of mechanical transduction. Previously, various techniques for measuring the mechanical force of cells have been developed in this field, including atomic force microscopy (AFM), traction force microscopy (TFM), micropillar arrays, magnetic twisting cytometry (MTC), optical tweezers, and molecular-tension-based fluorescence microscopy (MTFM) (Andreu et al., 2021; Combs et al., 2024; Guadarrama Bello et al., 2022; Lendenmann et al., 2019; Wu et al., 2018). Among these, MTFM was used to measure the mechanical forces through different tension probes. DNA with a unique structure is often used to create molecular tension probes, including TGT (Wang and Ha, 2013), digital tension probes (Zhang et al., 2014), six-helix-bundle DNA-origami tension probes (DOTPs) (Dutta et al., 2018), and so on. Ha team originally developed the TGT probes to control the force transmitted by cells (Wang and Ha, 2013). During specific cell binding to surface ligands, if the mechanical force exerted by the cells exceeds tension threshold (T_{tol}) of the strand, it will break, abolishing signal activation. The tether will endure and the signal can be successfully transmitted if the force remains below this threshold. Therefore, a series of strands with different T_{tol} values was designed to accurately measure the force needed to activate the signal (Li et al. 2021,

* Corresponding author.
E-mail address: yingsun@jlu.edu.cn (Y. Sun).

https://doi.org/10.1016/j.bios.2025.118324
Received 5 September 2025; Received in revised form 28 November 2025; Accepted 16 December 2025
Available online 17 December 2025

2023). While these excellent approaches are limited by expensive equipment and cumbersome functionalization steps. You team proposed a simple electrochemical method to measure cellular mechanical force (Amouzadeh Tabrizi et al., 2024). DNA-based tension probes are immobilized on a smartphone electrochemical device surface for the detection of tunable cellular mechanical forces at the pN scale. While live cells remain vulnerable to electrode contamination or interference from complex substrates at the screen-printed electrode interface. And the signal cannot be amplified. Therefore, it is necessary to develop a simple approach that avoids electrode contamination from complex substrates and combines amplification reaction for the measurement of pN forces with low-background signals and high sensitivity.

Electrochemiluminescence (ECL) is a light-emitting process where excited states are generated through electron transfer reactions between species produced electrochemically. This technology combines electrochemistry and chemiluminescence principles, providing high sensitivity, stability during operation, low background signals, and affordability (Li et al., 2023; Richter, 2004). These qualities have led to its application in fields like clinical diagnostics, food security (Zhou et al., 2025), and biological imaging (Meng et al., 2022) and so on. For measuring trace target substances, especially early disease biomarkers, highly sensitive ECL sensors have been developed with effective signal amplification techniques (Wang and Ha, 2013; Wu et al., 2025). As a result, various signal enhancement strategies have been adopted in ECL sensor design, including enzymatic catalytic amplification, photo-induced effects, and nucleic acid-based enzyme-free amplification technologies. Among these, enzyme-free catalytic amplification technologies like TSDR and CHA are widely used because of their high catalytic efficiency and strong

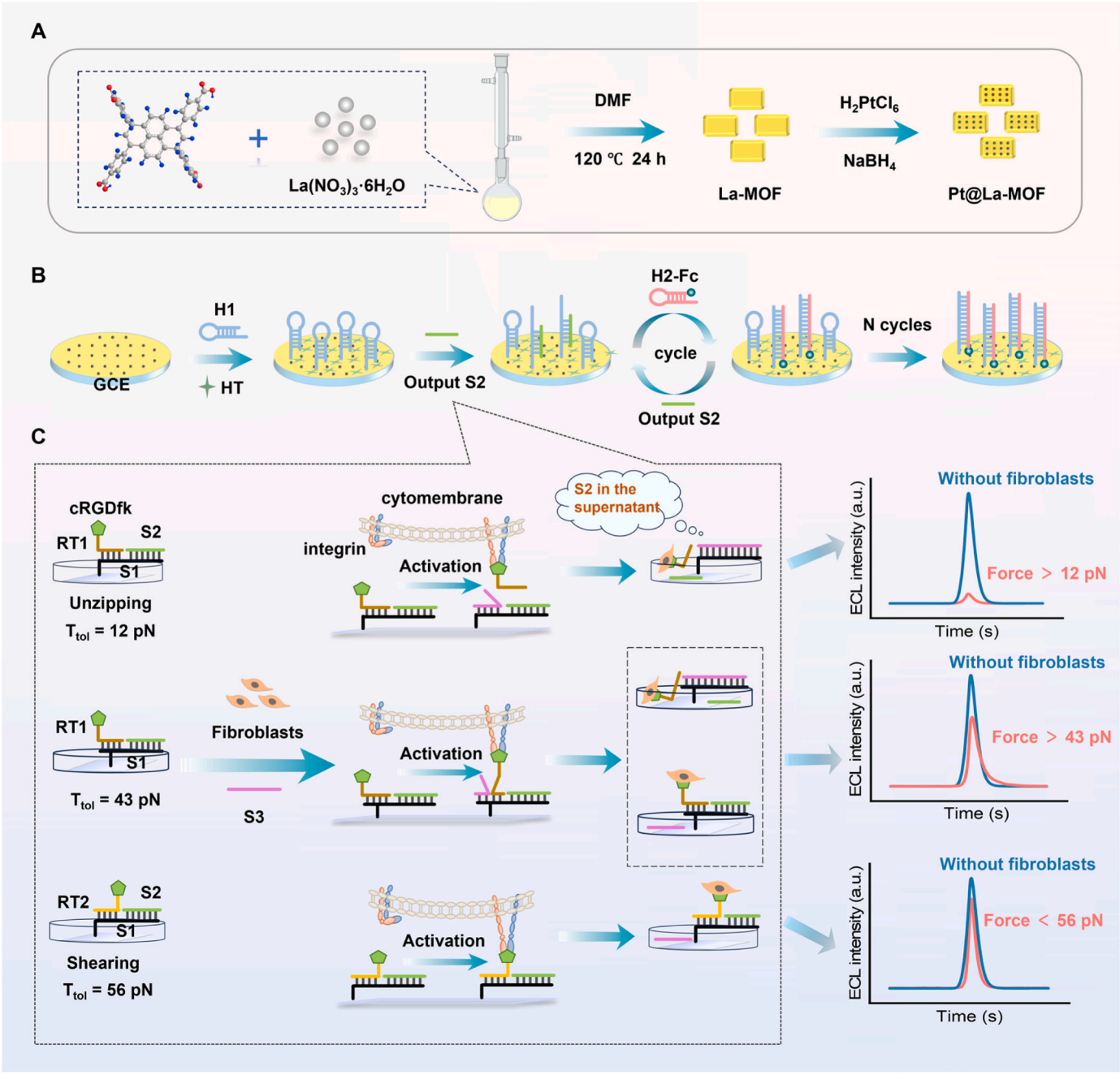

Scheme 1. The composition of the sensor and its response mechanism to fibroblasts mechanics. (A) Diagram for preparing Pt@La-MOF. (B) Fabrication steps of the ECL sensor. (C) The response of S1-S2-RT probes to pN-level cellular mechanical forces.

signal gain, which enhance detection sensitivity. Since receptor-mediated cellular force is transient and weak, making it difficult to quantify, one solution is to combine an amplification strategy with tension probe to measure the signal. The pN-level tension probe based on TGT, combined with an enzyme-free DNA signal amplification technique, enables the conversion of weak cellular force into a readily detectable ECL signal.

In ECL sensors, luminescent materials critically determine detection sensitivity. Metal nanoparticle (MNPs)/metal-organic frameworks (MOFs) composites, valued for improvement of ECL properties. MNPs are characterized by excellent electronic and optical properties. While MOFs are distinguished by distinct advantages arising from their ultra-high specific surface area, uniform structure, high porosity, and exceptional chemical stability. Novel nanomaterials created through the combination of MNPs and MOFs hold significant potential in sensing applications (Yang et al., 2017). Due to their unique antenna effect and self-luminescent property of lanthanide metal-organic frameworks (Ln-MOFs), these composites are considered strong candidates for ECL emission sensors. A ligand luminescence strategy was used to design the target material to improve the luminescence performance of Ln-MOFs. We employ TBAPy with ECL activity as the ligand, and synthesize La-MOF with lanthanide elements as the nodes. This material can stably and efficiently generate ECL signals. To further enhance the conductivity and loading capacity of La-MOFs, platinum nanoparticles (Pt NPs) were loaded onto their surface, successfully creating Pt@La-MOFs composite materials. Based on MNPs/MOFs composites, notable stability, and sensitivity improvements have been achieved in sensing performance.

In this study, a molecular TGT platform based on ECL was developed for measuring cellular mechanical force. In the ECL sensor, Pt@La-MOF was used as an emitter, and F-TSDR and CHA were employed as signal amplifiers (Scheme 1). When cells are incubated, integrins and other membrane receptors bind to the cRGDfK ligand on the double-stranded RT and exert force. The cellular mechanical forces exceeding T_{tol} will mechanically disrupt the hybridization of the DNA strands. In F-TSDR, cellular mechanical forces detach RT1 from S1, exposing toeholds that initiate S3-S1 hybridization and S2 release. The released S2 binds to electrode-immobilized H1, activating ECL through hairpin unfolding. The exposed catalytic domain then recruits H2-ferrocene (Fc) to form H1-H2 duplexes, reducing ECL and causing the signal to shift from the "on" to "off" state. The released S2 is cyclically reused, driving periodic ECL signal switching. If the cell mechanical force is below T_{tol} (RT2 stable at ~56 pN). It cannot trigger the structural denaturation of the S1-S2-RT2 probe to release S2, resulting in no ECL signal change. This work provides a new method on cellular mechanics measurement by utilizing readily detectable ECL signals. It is highly valuable for studying mechanical mechanisms to help us better understand cell growth, development and migration.

2. Experimental section

2.1. Materials and reagents

Additional details can be found in the supporting information (SI).

2.2. Construction process of the ECL sensor

The detailed experimental procedure for measuring cell mechanical force using ECL sensor is shown in Fig. S1 (the ECL step is cell-free).

3. Results and discussion

3.1. The design principle of TGT based on ECL sensor for measuring cellular mechanical force

Scheme 1 demonstrates the design principle of TGT based on the ECL sensor for measuring cellular mechanical forces. First, the Pt@La-MOF was prepared using the solvothermal method (Scheme 1A), then employed as anode luminescent unit to build the ECL sensing platform (Scheme 1B). Pt NPs not only facilitate electron transfer, with the strong ECL emission acting as the "signal on" state, but also capture and stabilize H1 through Pt-S binding. As shown in Schemes 1C, in the S1-S2-RT DNA tension probe, the tether between the S1 and RT parts breaks at the tension threshold, which is called T_{tol}. We specifically attach the S1-S2-RT to the slide substrate using biotin on S1 and avidin affinity (Scheme 1C). In the "unzipping" mode, the rupture force between S1 and RT1 in S1-S2-RT1 is about 12 pN (T_{tol} ~12 pN). In the "shearing" mode, the estimated rupture force between S1 and RT2 in S1-S2-RT2 is roughly 56 pN (T_{tol} ~56 pN). When the cell contacts the probe, integrin receptors on the cell membrane bind to the cRGDfk and exert tension on the ligand. The mechanical force greater than or equal to 12 pN causes RT1 in S1-S2-RT1 to detach from S1. Adding S3 present in the system would continue to trigger the F-TSDR process and produce a large amount of S2. The resulting supernatant rich in S2, is then extracted and introduced into the ECL sensing interface, where H1 is specifically activated and cooperates with H2-Fc to jointly initiate the CHA process (Scheme 1B). Many H2-Fc units are captured by the opened H1, effectively quenching the ECL signal ("signal off"), which is used to measure the greater than or equal to 12 pN cellular mechanical force. Conversely, in the "shearing" mode with T_{tol} roughly 56 pN of cellular mechanical force, most cell membrane receptors cannot afford forces reaching 56 pN. And they are less likely to cause RT2 in the DNA tension probe S1-S2-RT2 to detach from S1. H1 cannot be specifically activated by S2 and remains intact, resulting in only a slight decrease in the ECL signal. Thus, cellular mechanical forces with two different T_{tol} can be measured via ECL signal quenching.

3.2. Morphological and elemental characterization of Pt@La-MOF

Pt@La-MOF was synthesized using a simple "one-pot" method. The morphology of the synthesized La-MOF and Pt@La-MOF was characterized by scanning electron microscopy (SEM) and transmission electron microscopy (TEM). La-MOF shows a blocky structure with an edge length of 1.5 ± 0.5 μm (Fig. 1A). When Pt NPs are reduced onto the surface of La-MOF, a layer of small particles covers the surface of the nanoblocks compared to a single La-MOF (Fig. 1B), and the difference is notable. The assembly of Pt@La-MOF was further analyzed using UV–Vis and fluorescence (FL) spectroscopy (Fig. 1C and Fig. S2). The UV–Vis absorption spectrum of Pt@La-MOF showed two peaks at 325 and 442.5 nm, while its fluorescence spectrum had a single peak at 499.6 nm. This fluorescence peak exhibited a slight red shift compared to La-MOF, indicating an increase in size after nanoparticle loading.

Notably, X-ray diffraction (XRD) analysis shows that the diffraction pattern of the encapsulated Pt@La-MOF closely resembles that of the corresponding La-MOF and aligns well with the standard reference pattern (Fig. 1D). This suggests that the inherent crystalline framework of La-MOF has been preserved. Compared to the strong peaks from the related La-MOF, the peaks from PtNPs within the synthesized crystal are too weak to observe clearly, likely due to their low concentration or small size.

To further characterize the surface elemental composition and chemical valence states of Pt@La-MOF, X-ray photoelectron spectroscopy (XPS) was performed. The full XPS spectrum (Fig. 1E) displays characteristic double peaks of C 1s, O 1s, and La 3d at 284.66, 531.74, 838.16, and 855.23 eV, indicating the presence of C, O, and La in the composite material. The high-resolution XPS spectrum of Pt shows two distinct peaks at 71.16 and 74.97 eV, which are characteristic of the double peaks of Pt $4f_{5/2}$ and Pt $4f_{7/2}$. Thus, the formation of PtNPs on La-MOF was confirmed. In addition, Fourier transform infrared spectroscopy (FT-IR) was used to study the functional groups and structure of Pt@La-MOF (Fig. S3). The broad absorption peaks at 3438 cm^{-1} (A), 3417 cm^{-1} (B), and 3386 cm^{-1} (C) correspond to the hydroxyl vibration

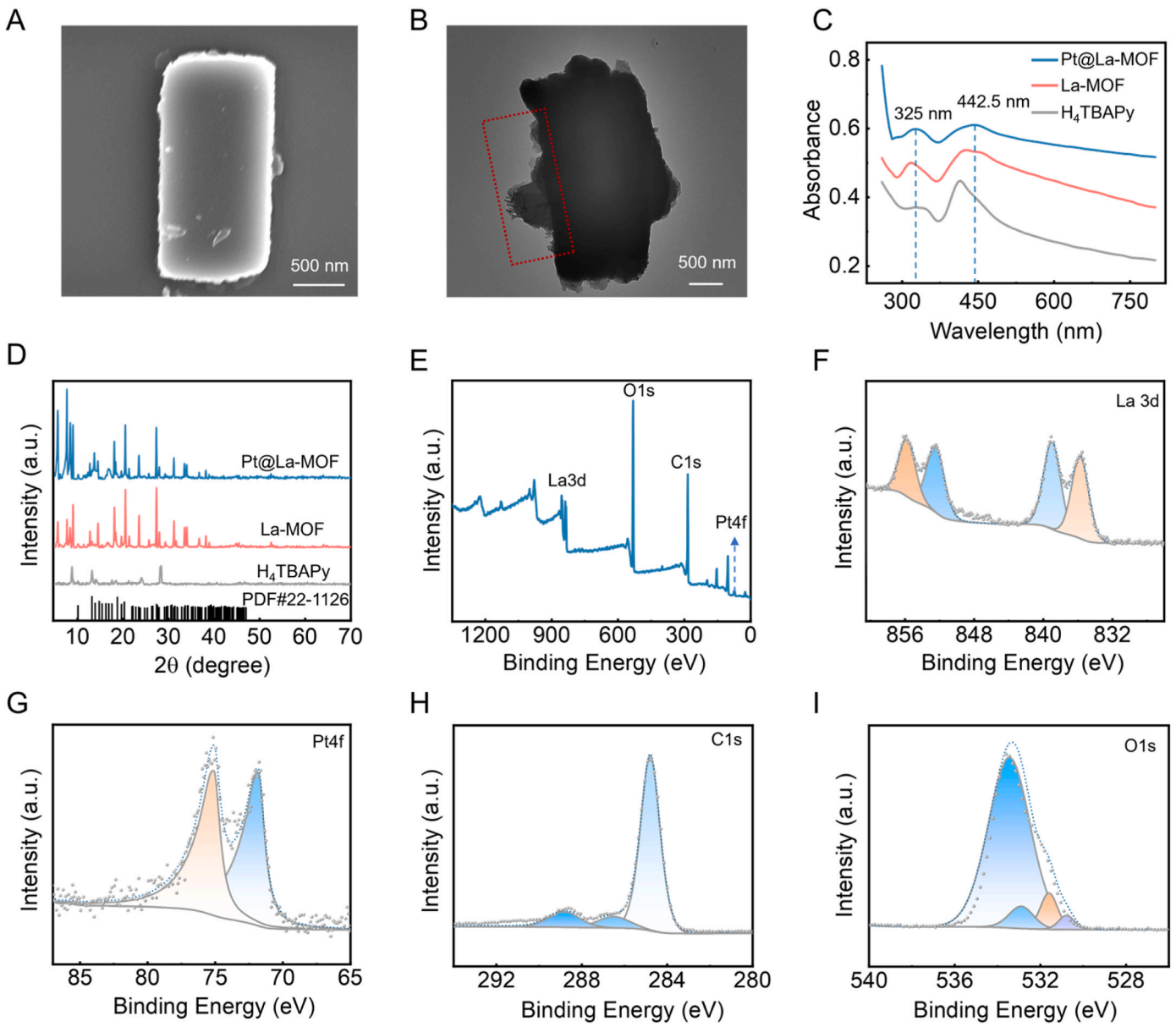

Fig. 1. Morphological and elemental characterization of Pt@La-MOF. (A) SEM image of La-MOF. Scale bar: 500 nm. (B) TEM image of Pt@La-MOF. Scale bar: 500 nm. (C) UV–vis absorption spectra of materials. (D) XRD spectra of materials. (E) XPS survey spectrum of Pt@La-MOF. (F) High-resolution XPS spectrum of La 3d, (G) Pt 4f, C 1s, and (I) O 1s.

of -COOH groups, while the carbonyl absorption peaks are at 1691 cm^{-1} (A), 1655 cm^{-1} (B), and 1605 cm^{-1} (C). The strong absorption bands at 1409 cm^{-1} (B) and 1407 cm^{-1} (C) relate to the vibration of the aromatic ring framework. A new absorption band appears at 1099 cm^{-1} in Pt@La-MOF. This suggests that new chemical bonds, similar to Pt-O, may have formed. These results confirmed the successful synthesis of Pt@La-MOF.

3.3. The possible ECLmechanism of Pt@La-MOF/TPrA

Compared with bare electrodes (Fig. S4A), the ECL spectrum of Pt@La-MOF exhibits a peak at 513.7 nm (Fig. 2A), whereas its photoluminescence (PL) spectrum displays a prominent peak at 499.6 nm (Fig. S2). These results suggest that the ECL and PL emissions of Pt@La-MOF originate from similar processes: ground-state excitation, excited-state formation, and radiative decay.

To explain the mechanism of the Pt@La-MOF/TPrA system, we recorded ECL responses from solutions containing La-MOF (curve a), La-MOF/TPrA (curve b), and Pt@La-MOF + TPrA (curve c) (Fig. 2B). After immobilizing water-dispersed La-MOF on a GCE, a weak ECL signal was observed (curve a). Upon immersing the GCE in TPrA solution, the ECL intensity increased significantly. This is mainly due to the reaction between TPrA (co-reactant) and Pt@La-MOF, which forms the excited state Pt@La-MOF*, leading to enhanced emission. Furthermore, Pt NPs in Pt@La-MOF have excellent conductivity and can interact with TPrA to produce additional TPrA* radicals. Similarly, curve c shows a significantly higher ECL intensity than curve b, because Pt-loaded La-MOF reduces the electron transfer distance and improves ECL efficiency.

The possible mechanism of the Pt@La-MOF/TPrA system is illustrated (Fig. 2C), along with the following equations:

$$Pt@La-MOF-e^{-}\rightarrow Pt@La-MOF^{+} \quad (1)$$

$$TPrA\text{–}e^{-}\rightarrow TPrA^{\cdot+} \quad (2)$$

$$TPrA^{\cdot+}\text{–}H^{+}\rightarrow TPrA^{\cdot} \quad (3)$$

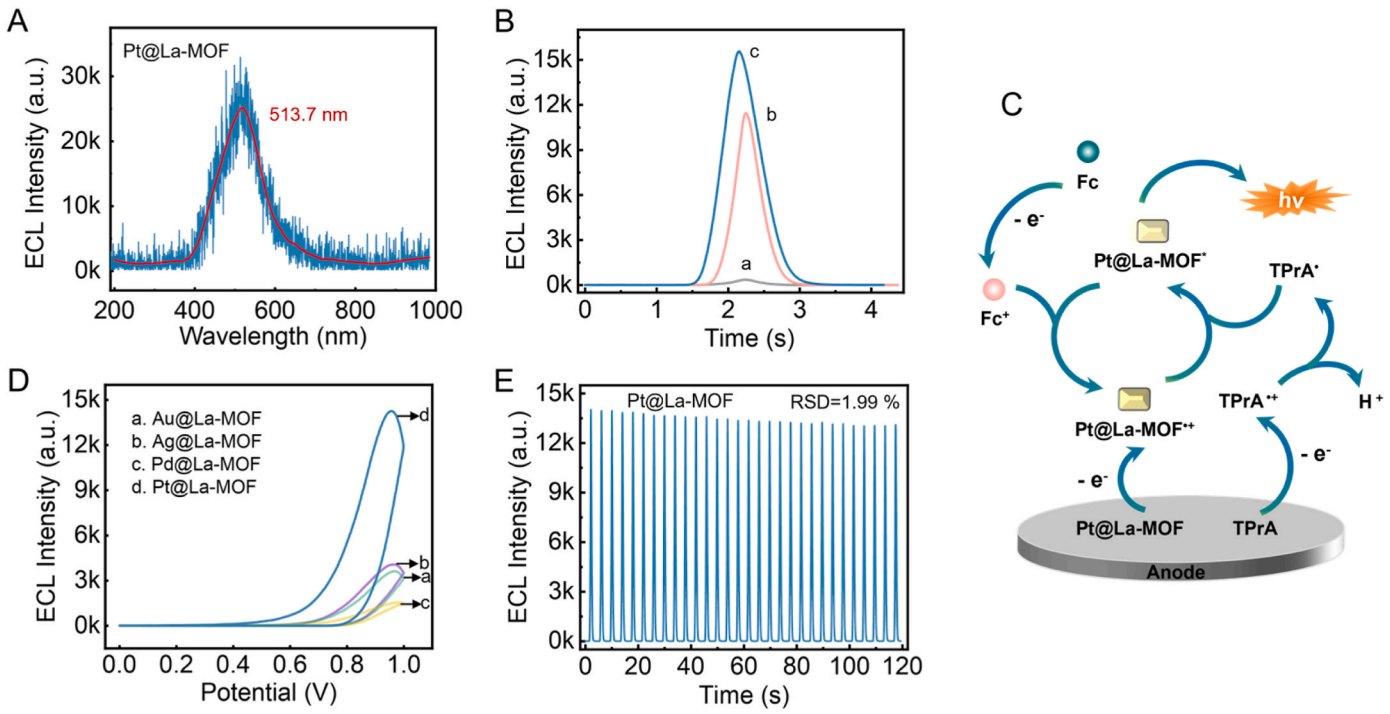

Fig. 2. The ECL properties of Pt@La-MOF. (A) ECL spectrum of Pt@La-MOF. (B) ECL intensity of different systems. (a) La-MOF in 10 mM PBS. (b) La-MOF in 4 mM TPrA. (c) Pt@La-MOF in 4 mM TPrA. (C) The mechanism of the Pt@La-MOF/TPrA system. (D) ECL intensity of (a) Au@La-MOF, (b) Ag@La-MOF, (c) Pd@La-MOF, and (d) Pt@La-MOF. (E) The ECL stability of Pt@La-MOF.

$$Pt@La-MOF^{\cdot+} + TPrA^{\cdot} \rightarrow Pt@La-MOF^{*} + Products \quad (4)$$

$$Pt@La-MOF^{*} \rightarrow Pt@La-MOF + h\nu \quad (5)$$

Notably, using the $[Ru(bpy)_3]^{2+}$/TPrA system as a reference (Φ_{ECL} = 100 %), Pt@La-MOF exhibits a high ECL efficiency (Φ_{ECL}) of 36 % (SI for details).

To further elucidate the mechanism underlying the enhancement of La-MOF/TPrA systems by Pt NPs, the effects of loading different precious metals (Au, Ag, Pd, and Pt) onto luminescent La-MOF were compared (Fig. 2D and Fig. S4B). Pt NPs exhibited a markedly stronger enhancement of the La-MOF/TPrA system than Au NPs, Ag NPs, or Pd NPs. Equations in the SI explain the proposed catalytic role of Pt NPs in the ECL system and the quenching mechanism of Fc toward the ECL signal.

Stability is a critical indicator for evaluating material performance. Fig. 2E displays the ECL signals of Pt@La-MOF after 30 consecutive cycles. The relative standard deviation (RSD) of the material is 1.99 %, which is lower than that of La-MOF (Fig. S4C), confirming the high stability of the Pt@La-MOF/TPrA system. Next, we assessed the aqueous-phase temporal stability of the material (Fig. S5A and S5C). Compared to the first day, the ECL signal on the tenth day decreased by only 13.4 % (1−12800/14775 a.u.). Additionally, we measured the ECL signal differences between batches of this luminescent material (Fig. S5B and S5D). The results show that it demonstrates excellent batch-to-batch stability.

3.4. Optimization of reaction conditions

To further explore the ECL performance of Pt@La-MOF in aqueous conditions, we first studied the effects of co-reactants. TPrA significantly boosted the ECL signal of Pt@La-MOF, while TEA did not show a notable improvement (Fig. S6A). Meanwhile, as the concentration of TPrA increased, the ECL signal steadily rose (Fig. S5C). Subsequently, the key experimental parameters were systematically optimized, including concentration, potential window, scan rate, and pH value (Fig. S7A–H). After considering multiple factors, TPrA was selected as the co-reactant. The optimal reaction conditions were: TPrA concentration at 4 mM, potential range from 0.0 to 1.0 V (relative to Ag/AgCl), scan rate at 0.5 V/s, and pH at 7.4. Furthermore, the ECL potential of Pt@La-MOF/GCE in 4 mM TPrA-containing PBS was measured (Fig. S8), focusing on ECL triggering (around 0.5 V) and peak potentials (about 1.0 V). The results indicated that the potential at maximum ECL intensity was 1.0 V, matching the previously optimized potential range.

3.5. Characterization of the ECL sensor

To verify the feasibility of the constructed ECL sensor, the step-by-step manufacturing process of the ECL sensor was confirmed using three methods: ECL, CV, and EIS. The bare GCE showed a weak ECL signal (Fig. 3A, curve b) and low current intensity (Fig. 3B, curve b) in TPrA (4 mM). When Pt@La-MOF was modified on the GCE surface (TPrA system), the ECL intensity increased significantly (15150 a.u. curve d), indicating that Pt@La-MOF is an excellent ECL emitter. The presence of H2-Fc caused a decrease in both ECL (1443 a.u.; Fig. 3A, curve e) and current signals (Fig. 3B, curve e).

As shown in Fig. 3C, two distinct redox peaks were observed for GCE in 5.0 mM $[Fe(CN)_6]^{3-}$ (curve a). Pt@La-MOF modification of the electrode surface decreased redox peak currents (curve b). Subsequent H1 addition further reduced the current (curve c) due to repulsive interactions between negatively charged DNA and the $[Fe(CN)_6]^{3-}$ redox couple. Introducing H1/S1/HT caused a further decrease in current (curve d), confirming blocking of non-specific electrode binding sites. The current decrease in curve e resulted from Fc-H2 hybridization with H1, which hindered electron transfer and repelled $[Fe(CN)_6]^{3-}$. These results confirm the successful assembly of the ECL sensor.

A small semicircle appears in the EIS of the bare electrode (curve a), indicating low impedance (Fig. 3D). When modified with Pt@La-MOF (curve b), the electrode impedance increases slightly. Modification with Pt@La-MOF/H1 (curve c) causes a clear expansion of the semicircle, showing a further rise in impedance. With Pt@La-MOF/H1/S2

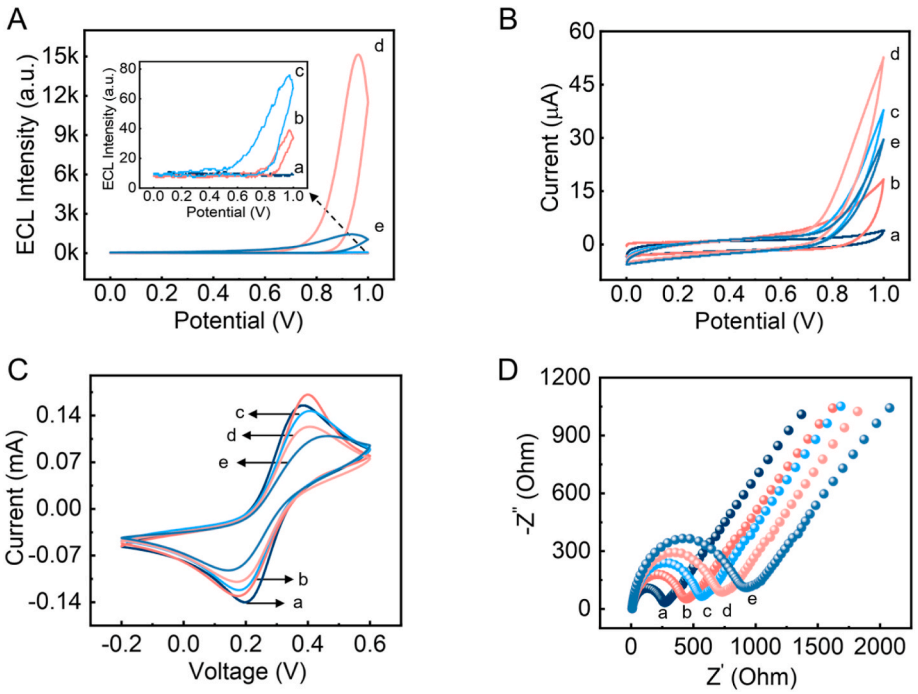

Fig. 3. Characterization of the force sensor construction process. (A) ECL signals and (B) CV of each step electrodes. (a) Bare GCE. (b) GCE + 4 mM TPrA (in 10 mM PBS). (c) GCE/Pt@La-MOF + 10 mM PBS. (d) GCE/Pt@La-MOF + 4 mM TPrA (in 10 mM PBS). (e) GCE/Pt@La-MOF/H2-Fc + 4 mM TPrA (in 10 mM PBS). (C) CV profile and (D) EIS monitors the fabrication process of the engineered biomechanical sensor in an electrolyte containing 5 mM $K_4[Fe(CN)_6]/K_3[Fe(CN)_6]$ and 0.1 M KCl. (a) Bare GCE. (b) GCE/Pt@La-MOF. (c) GCE/Pt@La-MOF/H1. (d) GCE/Pt@La-MOF/H1/HT/S2 (S2 is triggered by mechanical forces of greater than 12 pN). (e) GCE/Pt@La-MOF/H1/HT/S2/H2-Fc.

modification (curve d), impedance increases further. For the Pt@La-MOF/H1/H2-Fc-modified electrode (curve e), the solid loading of Fc on H2 hinders surface electron transfer, leading to increased electrode impedance. Based on the analysis of ECL, CV, and EIS, the assembly process of the ECL sensor proceeded as anticipated.

3.6. Measurement of cellular mechanical force with the ECL sensor

Before conducting the cellular mechanical force measurement, we used PAGE analysis to verify the feasibility of the F-TSDR and CHA testing methods (Fig. S9). These results clearly demonstrate that F-TSDR and CHA can be effectively used to construct the ECL sensor in this study. To measure whether the sensors manufactured can truly be used to measure cellular forces generated by fibroblasts, we first coated polyethylene glycolized coverslips with 12 pN, 43 pN, or 56 pN S1-S2-RT probes, and then added 500 μL of fibroblasts (10^8 cells/mL) to each system (Fig. 4A–C). First, we measure the ECL signals from the sensor with background signal and high sensitivity. As shown in Fig. 4D–I, after incubation and treatment at different times, it was observed that the ECL signals of the 43 pN and 56 pN sensors decreased slowly, and the extent of decrease was relatively mild. In contrast, the ECL signal of the 12 pN sensor decreased markedly with longer incubation times. To measure these ECL signals triggered by mechanical force more precisely, we introduced the relative change rate of ECL signal intensity (denoted as I%), with the calculation formula: $I\% = (I_0 - I_c)/I_0 \times 100\ \%$. Here, I_0 is the baseline ECL signal of the sensor when no fibroblasts are present, and I_c is the ECL signal value after fibroblasts incubation. After incubation with 500 μL of 10^8 fibroblasts/mL for 60 min, the I% of the 12 pN, 43 pN, and 56 pN sensors approximately 92.8 %, 35.9 %, and 29.9 %, respectively (Fig. 4G–I). The I% of ECL signals from 92.8 % to 29.9 % indicates a reduction in the number of output chains S2 under the influence of various mechanical forces. After the sensor system was incubated with fibroblasts, the sensor with $T_{tol} = 12$ pN could rupture and release more S2. While, force generated by fibroblasts rarely reaches 56 pN to rupture the shearing mode and the ECL signals decrease relatively mild. The differential ECL signals observed across tension probes (12, 43, and 56 pN) arise from force-driven S2 release governed by probe mechanical stability and its effect on CHA kinetics. The 12 pN probes undergo sustained rupture under persistent cellular tension, releasing more S2 and accelerating CHA-driven ECL quenching. In contrast, 43 and 56 pN probes experience limited or transient force application, restricting S2 release and resulting in weaker signal attenuation, particularly as few fibroblasts exert forces approaching the 56 pN upper limit.

Subsequently, we aim to evaluate the sensitivity of the ECL sensor by measuring the mechanical force from different cell numbers. Using the 12 pN sensor as example, we cultured 10^2, 10^3, 10^4, 10^5, 10^6, 10^7, and 10^8 fibroblasts/mL on a polyethylene glycol-coated cover glass for 60 min. Subsequently, a significant decrease in the relative ECL signal intensity of 10.8 %, 17.7 %, 37.1 %, 53.0 %, 58.1 %, 79.6 %, and 93.2 % was observed (Fig. 5A). The ECL sensor can indeed be used to measure the force generated by a small number of cells. The ECL intensity exhibits a strong linear relationship with the logarithm of the cell concentration (Fig. 5B). The linear equation is $I = -1994.15 \lg c + 17066.49$ ($R^2 = 0.9986$).

Furthermore, to assess the stability of the sensor, we performed 10 cycles of continuous potential measurements with 500 μL of 10^3, 10^4, 10^7, and 10^8 cells/mL. As shown in Fig. 5C, the ECL signal displayed no significant fluctuations. The RSD for 10^3 cells/mL was 0.84 %, 10^4 cells/mL was 1.15 %, 10^7 cells/mL was 1.06 %, and 10^8 cells/mL was 0.77 %. Figs. S9 and S10 demonstrate the high selectivity and reproducibility of the cell mechanical force sensor.

To validate the use of the ECL sensor for assessing pharmacological effects on cellular force, dose-response studies were performed using blebbistatin (a myosin II ATPase inhibitor that reduces contractility) and thrombin (a serine protease enzyme that enhances contraction). At a constant cell density, incubation with 10–40 μM blebbistatin significantly increased ECL intensity (Fig. S10), consistent with its role in

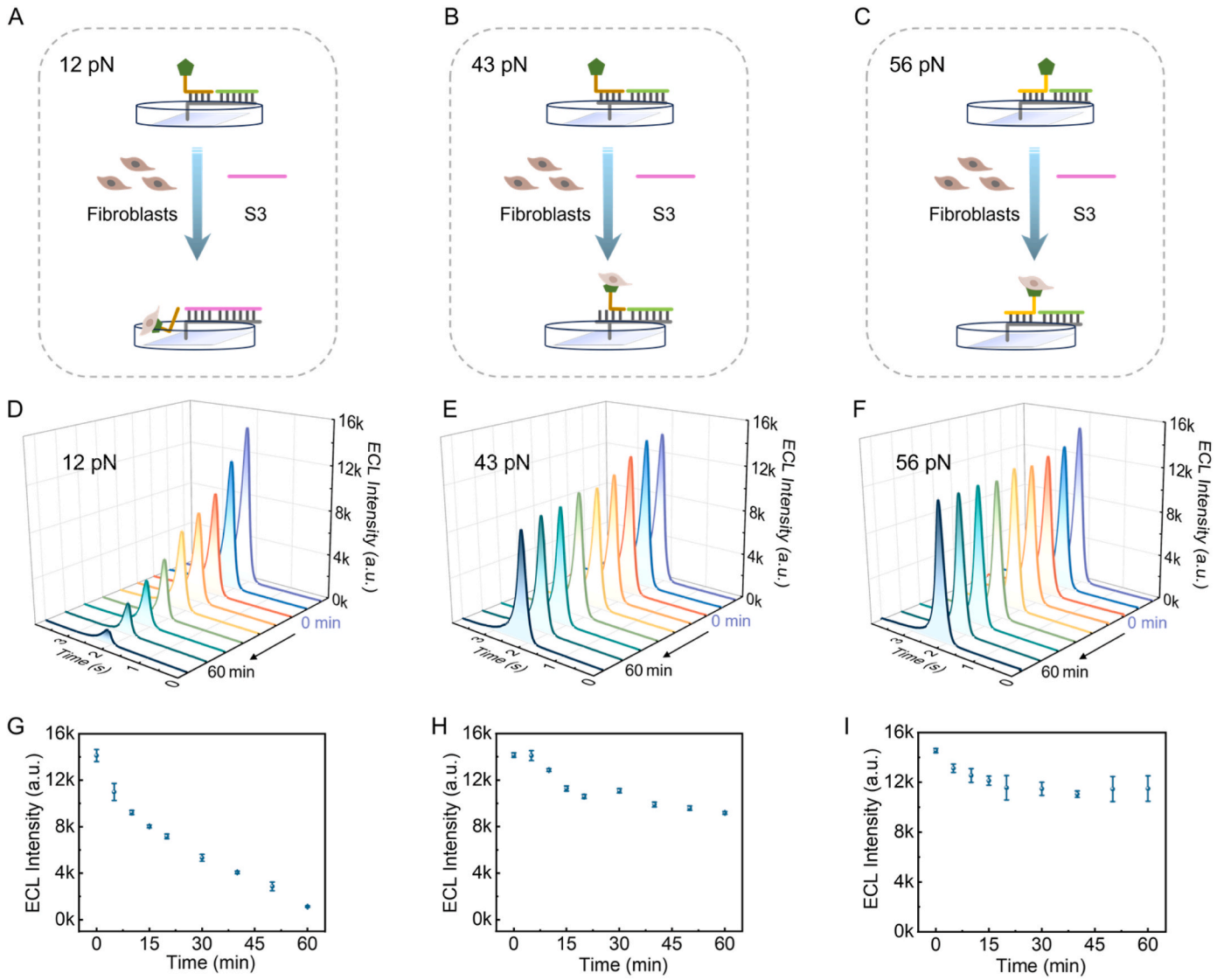

Fig. 4. The ECL signals are triggered by mechanical forces from cells at different pN levels. A schematic diagram of the F-TSDR process induced by cellular mechanical forces of (A) 12 pN, (B) 43 pN and (C) 56 pN. The response of the ECL sensor to various pN levels and incubation times at the same cell concentration. (D) 12 pN. (E) 43 pN. (F) 56 pN. The incubation times were 0, 5, 10, 15, 20, 30, 40, 50, and 60 min, respectively. (G), (H) and (I) are scatter plots corresponding to Fig (D), (E), and (F), respectively (mean ± SD, n = 3).

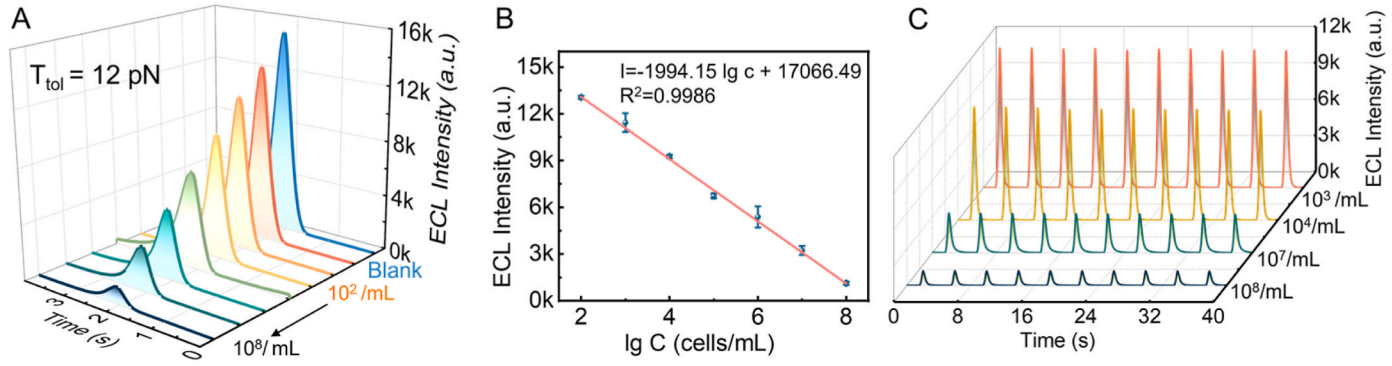

Fig. 5. Performance of the sensor of the cellular mechanical force. (A) ECL response corresponding to different concentrations of fibroblasts. (B) The corresponding calibration curves of (A) (error bars = SD, n = 3). (C) The stability of the force sensor under different concentrations of fibroblasts.

inhibiting actin-myosin interaction. Conversely, the thrombin (10, 30 μM) markedly decreased the signal (Fig. S11), indicating that it promotes the expression of cell adhesion molecules and enhances the contractile force of fibroblasts.

4. Conclusions

In summary, the TGT platform based on an ECL sensor translates cellular mechanical forces into quantifiable ECL signal transitions. A cellular mechanical force of approximately 12 pN induced a transition of the ECL sensor from signal "on" to "off", whereas a force threshold around 56 pN prevented significant ECL quenching. This design not only confirms the sensor's ability to discriminate between distinct cellular mechanical forces but also demonstrates high sensitivity. By incorporating Pt@La-MOF emitters, F-TSDR, and CHA amplification, the platform establishes a new paradigm for mechanobiology. Moreover, the ECL intensity shows a strong linear relationship with the logarithm of cell concentration. Future applications may include dynamic force mapping during cellular migration or real-time evaluation of drug efficacy, making this technology a versatile complement to existing biomechanical tools. While this study is limited by its reliance on simplified in vitro substrates, which constrains spatial resolution. More importantly, the mechanical properties of cells cultured on these artificial matrices do not fully replicate the structural anisotropy and viscoelasticity in vivo. Future efforts should focus on developing more physiologically relevant culture substrates that better mimic native microenvironments, thereby improving biological relevance and measurement accuracy.

CRediT authorship contribution statement

Xiaofei Ma: Writing – original draft, Validation, Methodology, Investigation, Conceptualization. **Chen Zhao:** Investigation, Data curation. **Yongli Wu:** Data curation, Conceptualization. **Zhuoxin Ye:** Formal analysis, Data curation. **Pinyi Ma:** Resources, Funding acquisition. **Daqian Song:** Resources, Project administration, Funding acquisition. **Ying Sun:** Writing – original draft, Methodology, Investigation, Formal analysis, Conceptualization.

Declaration of competing interest

The authors declare that they have no known competing financial interests or personal relationships that could have appeared to influence the work reported in this paper.

Acknowledgements

This work was supported by the National Natural Science Foundation of China (22074052 and 22004046) and the Science and Technology Developing Foundation of Jilin Province of China (20230101033JC).

Appendix A. Supplementary data

Supplementary data to this article can be found online at https://doi.org/10.1016/j.bios.2025.118324.

Data availability

Data will be made available on request.

References

Amouzadeh Tabrizi, M., Bhattacharyya, P., Zheng, R., You, M., 2024. Biosens. Bioelectron. 253, 116185.
Andreu, I., Falcones, B., Hurst, S., Chahare, N., Quiroga, X., Le Roux, A.-L., Kechagia, Z., Beedle, A.E.M., Elosegui-Artola, A., Trepat, X., Farré, R., Betz, T., Almendros, I., Roca-Cusachs, P., 2021. Nat. Commun. 12 (1).
Combs, J.D., Foote, A.K., Ogasawara, H., Velusamy, A., Rashid, S.A., Mancuso, J.N., Salaita, K., 2024. J. Am. Chem. Soc. 146 (33), 23034–23043.
Dutta, P.K., Zhang, Y., Blanchard, A.T., Ge, C., Rushdi, M., Weiss, K., Zhu, C., Ke, Y., Salaita, K., 2018. Nano Lett. 18 (8), 4803–4811.
Elosegui-Artola, A., Oria, R., Chen, Y., Kosmalska, A., Pérez-González, C., Castro, N., Zhu, C., Trepat, X., Roca-Cusachs, P., 2016. Nat. Cell Biol. 18 (5), 540–548.
Guadarrama Bello, D., Moraille, P., Boughari, S., Badia, A., Nanci, A., 2022. Mater Today Bio 14.
Hu, Y., Duan, Y., Salaita, K., 2023. Angew. Chem. Int. Ed. 62 (30).
Huse, M., 2017. Nat. Rev. Immunol. 17 (11), 679–690.
Jimbo, K., Konuma, T., Ito, T., Nakajima-Takagi, Y., Iwama, A., Tojo, A., 2020. Blood 136 (Suppl. 1), 23–24.
Lendenmann, T., Schneider, T., Dumas, J., Tarini, M., Giampietro, C., Bajpai, A., Chen, W., Gerber, J., Poulikakos, D., Ferrari, A., Panozzo, D., 2019. Nano Lett. 19 (10), 6742–6750.
Li, H., Zhang, C., Hu, Y., Liu, P., Sun, F., Chen, W., Zhang, X., Ma, J., Wang, W., Wang, L., Wu, P., Liu, Z., 2021. Nat. Cell Biol. 23 (6), 642–651.
Li, M., Li, Z., Wang, P., Ma, Q., 2023. Biosens. Bioelectron. 228, 115225.
Medina, E., Easa, Y., Lester, D.K., Lau, E.K., Sprinzak, D., Luca, V.C., 2023. Nat. Commun. 14 (1), 891.
Meng, C., Knežević, S., Du, F., Guan, Y., Kanoufi, F., Sojic, N., Xu, G., 2022. eScience 2 (6), 591–605.
Moog, K.E., Barz, M., Bartneck, M., Beceren-Braun, F., Mohr, N., Wu, Z., Braun, L., Dernedde, J., Liehn, E.A., Tacke, F., Lammers, T., Kunz, H., Zentel, R., 2016. Angew. Chem. Int. Ed. 56 (5), 1416–1421.
Richter, M.M., 2004. Chem. Rev. 104 (6), 3003–3036.
Sun, Z., Costell, M., Fässler, R., 2019. Nat. Cell Biol. 21 (1), 25–31.
Wang, X., Ha, T., 2013. Science 340 (6135), 991–994.
Wu, P.-H., Aroush, D.R.-B., Asnacios, A., Chen, W.-C., Dokukin, M.E., Doss, B.L., Durand-Smet, P., Ekpenyong, A., Guck, J., Guz, N.V., Janmey, P.A., Lee, J.S.H., Moore, N.M., Ott, A., Poh, Y.-C., Ros, R., Sander, M., Sokolov, I., Staunton, J.R., Wang, N., Whyte, G., Wirtz, D., 2018. Nat. Methods 15 (7), 491–498.
Wu, Y., Ye, Z., Chen, Y., Zhang, Y., Liu, R., Ma, P., Song, D., 2025. ACS Sens. 10 (8), 6231–6240.
Yang, D., Liu, X., Ma, J., Cui, B., Wang, Y., Xu, J., Zhang, Y., Ding, H., Wang, D., Liu, Q., Zhang, F., 2025. ACS Nano 19 (2), 2651–2664.
Yang, Q., Liu, W., Wang, B., Zhang, W., Zeng, X., Zhang, C., Qin, Y., Sun, X., Wu, T., Liu, J., Huo, F., Lu, J., 2017. Nat. Commun. 8 (1), 14429.
Zhang, Y., Ge, C.H., Zhu, C., Salaita, K., 2014. Nat. Commun. 5 (1), 5167.
Zhong, B.L., Lee, C.E., Vachharajani, V.T., Bauer, M.S., Südhof, T.C., Dunn, A.R., 2023. Nano Lett. 23 (20), 9187–9194.
Zhou, Y., Liu, S., Yan, X., Wei, Y., Ma, L., Yuan, R., 2025. Food Chem. 485, 144339.